Materials & Design 223 (2022) 111174

Contents lists available at ScienceDirect

Materials & Design

journal homepage: www.elsevier.com/locate/matdes

Gas-tight means zero defects - design considerations for thin-walled fluidic devices with overhangs by laser powder bed fusion

Fabian Grinschek [a,*], Amal Charles [b], Ahmed Elkaseer [b,c], Christoph Klahn [d], Steffen G. Scholz [b,e], Roland Dittmeyer [a]

[a] Institute for Micro Process Engineering (IMVT), Karlsruhe Institute of Technology (KIT), 76344 Eggenstein-Leopoldshafen, Germany
[b] Institute for Automation and Applied Informatics (IAI), Karlsruhe Institute of Technology (KIT), 76344 Eggenstein-Leopoldshafen, Germany
[c] Department of Production Engineering and Mechanical Design, Faculty of Engineering, Port Said University, Port Fuad 42526, Egypt
[d] Institute for Mechanical Process Engineering and Mechanics (MVM), Additive Manufacturing for Process Engineering (AMPE), Karlsruhe Institute of Technology (KIT), Germany
[e] Future Manufacturing Research Institute, College of Engineering, Swansea University, Swansea SA1 8EN, UK

HIGHLIGHTS

- Different methods for leak detection are presented and used dependent on defect density.
- Laser scan strategy for thin-walled overhangs is developed.
- It is possible to print gas-tight 30° overhangs below d_{Wall} < 300 µm, despite the low fault tolerance of this measure.
- Design and repeatability are critical.
- Case study shows the practical application of the findings for a distillation device.

GRAPHICAL ABSTRACT

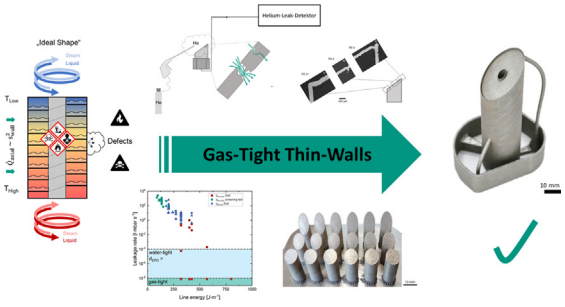

ARTICLE INFO

Article history:
Received 9 June 2022
Revised 12 September 2022
Accepted 18 September 2022
Available online 20 September 2022

Keywords:
Laser powder bed fusion
Thin walls
Gas-tight
Water-tight
Leak detection
Effects of defects

ABSTRACT

The industrial adoption of additive manufacturing (AM) technologies increased due to more applications and use cases demonstrating significant functional benefits. Additive manufacturing of thin-walled gas-tight structures with complex shapes can fulfil requirements for a wide range of applications, such as process equipment for the chemical industry. The requirement to be gas-tight makes the manufacturing process very fault-sensitive as even a single open pore in the submicron range can lead to an impermissible leak of hazardous gases. Further, it has always been a challenge to make thin walls using Laser Powder Bed Fusion of Metals (PBF-LB/M). We explore the key design limit of inclined overhanging gas-tight thin walls made from 316l. A double pass scan strategy is presented to realize these structures along with guidelines to be followed when attempting to print these structures. The paper reports the common failure modes where leaks occur and lessons learned to successful design and printing of gas-tight walls. The results show that fabrication of gas-tight walls is feasible even for a 30° inclination angle to the horizontal and wall thicknesses in the range of 200–300 µm. A case study shows the successful the application of the findings to the production of modular distillation devices.

1. Introduction

Additive manufacturing (AM) technologies offer benefits such as the ability to fabricate complex shapes without much additional

* Corresponding author.
E-mail addresses: fabian.grinschek@kit.edu (F. Grinschek), amal.charles@kit.edu (A. Charles), ahmed.elkaseer@kit.edu (A. Elkaseer), christoph.klahn@kit.edu (C. Klahn), steffen.scholz@kit.edu (S.G. Scholz), roland.dittmeyer@kit.edu (R. Dittmeyer).

https://doi.org/10.1016/j.matdes.2022.111174
0264-1275/

effort, reduced lead times, enhanced functionalities, etc., that have allowed their larger adoption and success by aerospace, automotive, and many other industries [1–3]. One further field for successful application of the advantages of AM already shown in these industries could be the chemical industry. Especially the fabrication of compact, high-performance devices for modular chemical plants could benefit from components being additively manufactured [4–8]. These devices are often characterized by a multitude of fine internal flow structures. As a result, heat transfer and mass transfer transversal to the flow direction are greatly accelerated, and this often enables step-change improvements in productivity or increased selectivity, or both, and at the same time improved control of the process in the device [9]. Conventionally, microfluidic devices are manufactured by rather costly methods such as etching, milling, diffusion bonding, and laser welding [9,10]. AM technologies complement or substitute these methods and can reduce the production costs and the lead times.

A potential use case are highly efficient distillation units for the refining of Power-to-X fuels likes synthetic kerosene or methanol in container-based plants. A design based on early concepts of Podbilinak seems a promising candidate [11]. Initially the apparatus design was not implemented due to the prohibitive costs of conventional manufacturing [12,13]. Its basic principle is a countercurrent flow of liquid condensate and evaporated steam in a spiral channel with low inclination angles. The pitch of the helix is in the range of a few millimeters to increase the flow path per height (as shown in Fig. 1 (a)).

Thermal management is a challenge in the design of such small distillation units [14,15]. The thermal dimensioning of the apparatus indicated that the manufacturing limits of the PBF-LB/M process need to be extended. A wall thickness of the apparatus well below 1 mm reduces the heat flow along the walls and maintains a high temperature gradient. A high space utilization for the flow channels is thereby also reached. The requirement for thin walls is in contrast to the current design guidelines for engineers and designers for PBF-LB/M additive manufacturing of stainless steel 316l (1.4404, X2CrNiMo17-12–2), a typical material for chemical process equipment. A typical recommendation for stable defect-free printing is a wall thicknesses of at least 1 mm [16]. There are studies investigating PBF-LB/M single track printing of thin walls on simple test geometries [17,18]. Clijsters et al. proposed a scan strategy for different geometries [19]. Wu et al. recently showed the limits of thin walls in the range of a few hundred microns [20]. The repeatable feasible limit is often reported to be approx. 0.3 mm [21–23] albeit with a potential risk of defects [16]. These limits are further influenced by the limited repeatability and stability of the PBF-LB/M process due to a variety of process parameters impacting the quality [23–26]. Riese et al. recently confirmed this need when comparing conventionally to additive manufactured packings for distillation [27].

The design of the distillation apparatus includes overhanging surfaces. Metal AM processes are known for issues with surface quality and mechanical properties of inclined surfaces even for thick-walled structures [28]. First, the transfer of heat from the part to the build platform is limited in overhanging situations. This is because no solid material connects the overhanging region and the build platform, causing overheating of the melt pool leading to dross formation on the down-skin surface and other defects [1,2,29,30]. In addition, thin walls are prone to distortions [20,24,31,32].These issues of inclined surfaces are usually prevented through either the usage of support structures [33] or through reorientation and repositioning of the part in the build chamber to avoid critically inclined surfaces [30,34]. The usage of support structures on our distillation device is practically impossible, because removing support structures from such thin walls would damage the part or at least deteriorate the quality of the AM part. Therefore, a "good" AM design as of today is driven by this restriction and not by the actual optimal flow shape [35]. The strategy can also be used here, to enlarge the angle by tilting the helical channel by e.g. 45° towards the horizontal build platform as shown in Fig. 1 b). In order to keep the functionality, it is then necessary to install the apparatus with a rotation of 45° in the final assembly of the application (as shown in Fig. 1 (c)).

The requirement for leak-tightness independent from the inclination angle is health and safety critical. The target application uses highly flammable and even toxic process media at the boiling

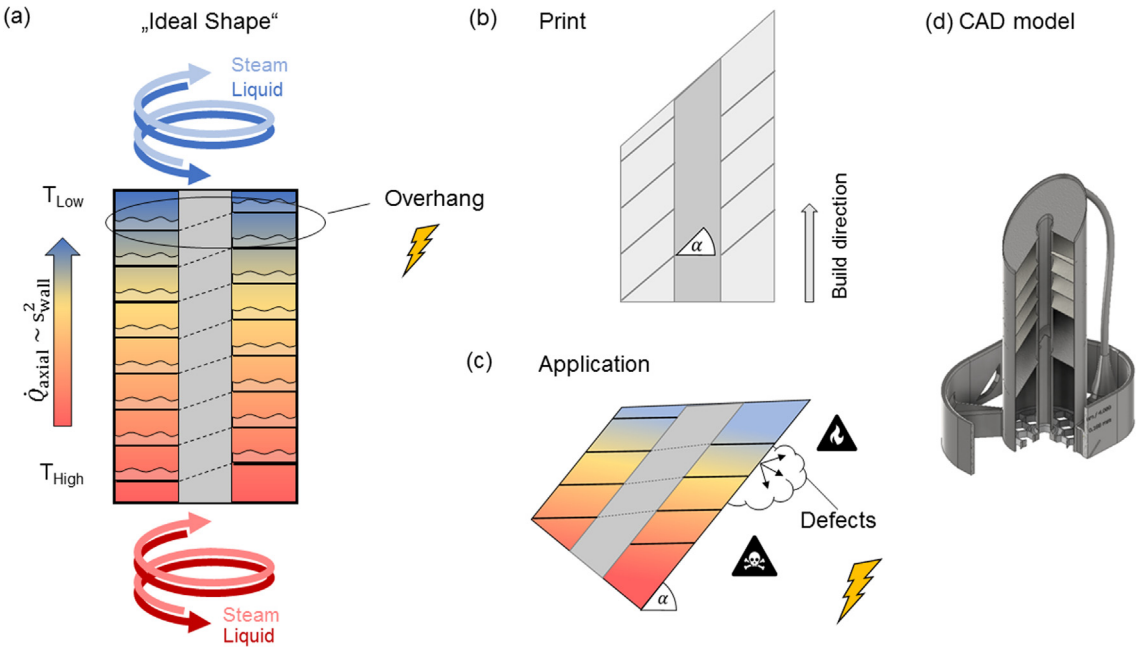

Fig. 1. (a) Ideal shape of a spiral distillation column inspired by Podbilinak [11]. (b) To increase the inclination angle of the overhangs, a tilt of the spiral could be used. (c) In the application, this results also in a tilt of the apparatus. (d) First CAD-draft of the apparatus with connectors.

point. This effectively requires the absence of any open porosity. To date, there are no investigations of AM technologies reported in literature which focus on freedom from leaks for thin-walled parts. As our application shows, there is a clear need for further research on the prevalence of leaks in thin walls. This study expands the "effects of defects" -research to effects other than mechanical ones [36,37]. If the minimum inclination angle and wall thickness could be lowered with still a reasonable process stability, the advantages of AM over conventional manufacturing could be exploited much more broadly. Consequently, we focus in this study on the combination of both critical features – reproducible manufacturing of thin-walled overhangs fulfilling the requirement of gas-tightness. We have developed a systematic approach to identify the limits and, afterwards, optimize the laser scanning strategy to print thin-walled gas-tight inclined overhangs. One of the main goals was to show a lower limit for the wall thickness with the conflicting priorities of thin-walls and low defect density. A Helium leak detector was used to find leaks, indicating pores with a diameter below 1 μm.

The AM literature describes various challenges on PBF-LB/M parts and recommends techniques to optimize the PBF-LB/M process [38–44]. This study follows a Design of Experiments (DoE) methodology with a two-step DoE approach consisting of a screening step to identify a suitable process window, followed by step of experimental trials to systematically quantify the effect of process parameters and their interactions on the process responses. The part properties of interest for the application in (internally) structured devices for modular chemical plants are the resulting wall thickness and chance of a defect.

2. Materials and methods

Fig. 2 illustrates the principal workflow of the parameter identification. First, small samples described in section 2.1 with a surface inclination of 30° to the horizontal were printed and a fast screening test of the water leaking rate (section 2.2) was conducted to identify the process range. With the process range, a second experimental plan identified promising parameter sets. These were then tested for repeatability with a Helium leak detector. The inclination and apparent wall thickness were varied to come to design recommendations. A full device was printed with the identified optimal set of parameters to demonstrate the applicability of the results for complex parts.

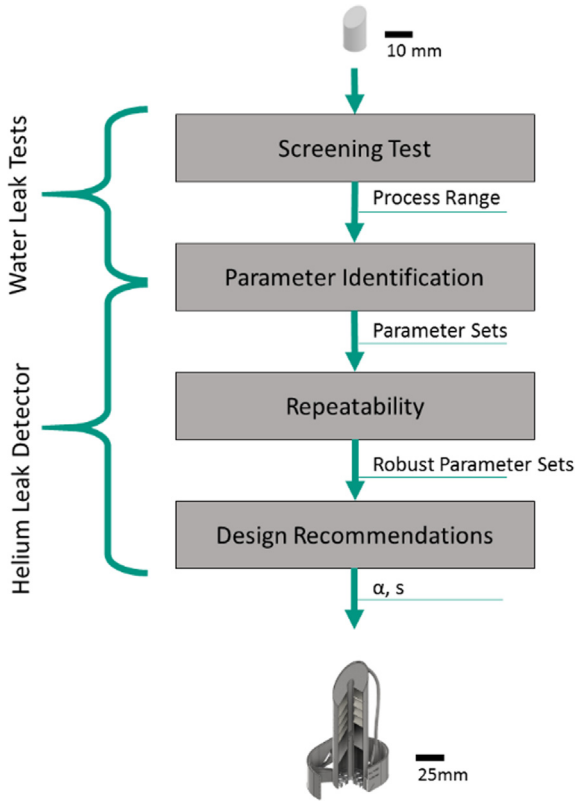

Fig. 2. Principal flow scheme of the investigation.

2.1. Specimens

Inspired by the draft of the design for the later device (Fig. 1), hollow cylinders with a nominal external diameter of 10.2 mm, with inclined top surfaces were designed as test specimens (see Fig. 3). The nominal wall thickness was chosen so that the distance between the inner and outer contour was 180 μm everywhere. Thereby the nominal wall thickness perpendicular to the surface is dependent on the inclination angle, which is intended for the scan strategy (section 2.3). The CAD model was created using Inventor 2021 (Autodesk, USA) and exported using the internal STL converter. Metallic tube fittings (Swagelok, USA) connect the specimens to the leak detector. A circular base with a wall thickness of 1 mm and a height of 10 mm was added to provide enough stiffness for the ferrules. The circular base (black shaded in Fig. 3 (a)) was printed with standard build parameters recommend by the manufacturer for stainless steel 316l. The leak tests showed no leaks there, thereby the evaluation of the leak rate of thin-walled structures is not influenced by the circular base. Before attaching the ferrule, the circular tube connection was machined to 10.0 mm. The parameters for the thin-walls (green shaded in Fig. 3 (a)) are given in section 2.3 and 2.5.

2.2. Characterization

The leak rate was tested with different methods depending on the expected number of leaks per unit area. To assess the general print quality, the surface roughness of the up-skin surface of the samples was measured. Furthermore, on selected samples the wall thickness was determined by cross cuts.

2.2.1. Leak rate

For a quick screening of the samples, 1 ml of water was filled into the samples (turned by 180°), and the time it took for

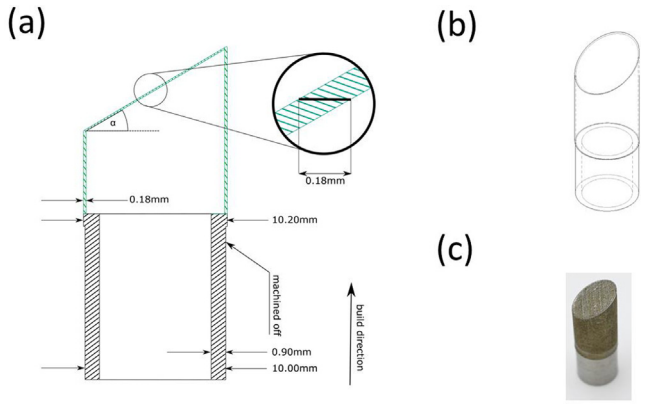

Fig. 3. (a) Drawing of the test specimen including the circular base for connection with a tube fitting. The areas in which the laser parameters were varied are marked in green. As show in the detail view, regardless of the angle α the distance between the inner and outer contour line is kept at 0.18 mm. (b) side view of the samples (c) image of a 30°-samples with machined circular base.

0.80 ml to drip through the samples was measured using a stop watch and a precision scale (compare also Fig. 4(a)). This test is especially suitable for test samples with many defects and a high permeability and allows a fast and simple first screening of the samples. Here the parameter sets that did not show any noticeable liquid penetration in the test over 18 min were classified as nearly tight (nearly defect-free). However, this test is not capable of testing samples for small leaks, since the leak rate is smaller than the evaporation rate. With the shortlisted parameters, further test specimens were printed for further investigations. Helium leak tests with the spray technique were conducted with a Helium-Leak detector (PhoeniXL, Leybold, Germany). The samples were connected to the detector and evacuated. Then the samples were sprayed with Helium gas from the outside as shown in Fig. 4 (b). If there is a leak, then the flow of Helium into the samples is detected with a highly sensitive mass spectrometer. With this technology, pores in the range of 100 µm down to a few nanometers can be detected [45]. Due to the small size of the defects the leak rate generally is an integral measurement value, meaning that the leak rate cannot be attributed to one specific defect or position. Hence, to check if the leak rate is from one or more defects, the samples were tested with nitrogen under water as shown in Fig. 10. Parts with a leak rate below 10^{-4} l mbar s^{-1} are denoted as liquid-tight and below 10^{-8} l mbar s^{-1} as gas-tight[45].

The water and Helium leak rates can be converted into each other - at least the order of magnitude - with equation (Eq. (1)).

$$q_{\mathrm{He},H_2O} \approx \frac{\mu_{H_2O}}{\mu_{He}} \cdot \frac{\Delta p_{H_2O}}{(p_1^2 - p_2^2)_{He}} \cdot q_{H_2O} \quad (1)$$

where q_{He,H_2O} denotes the converted leak rate for Helium, q_{H_2O}, the leak rate of water, μ_{H_2O} the viscosity of water, μ_{He} the viscosity of Helium, Δp_{H_2O} the pressure difference of water, p_1 the pressure in the front and p_2 the pressure behind the leak for the Helium measurement, respectively. [45,46] The values used for the conversion are given in Table 1.

From the standard Helium leak rate, a characteristic equivalent leak hole diameter d_{ELD} can be estimated by Eq. (2) assuming that the Helium flow is determined by the speed of sound in the smallest diameter [45]. The Helium flow of all defects in the sample is thereby attributed to the flow through one fictitious pore of the calculated diameter.

$$d_{ELD} \approx \sqrt{q_{L,\,measured}} \cdot 10^{-4}\,\mathrm{m} \quad (2)$$

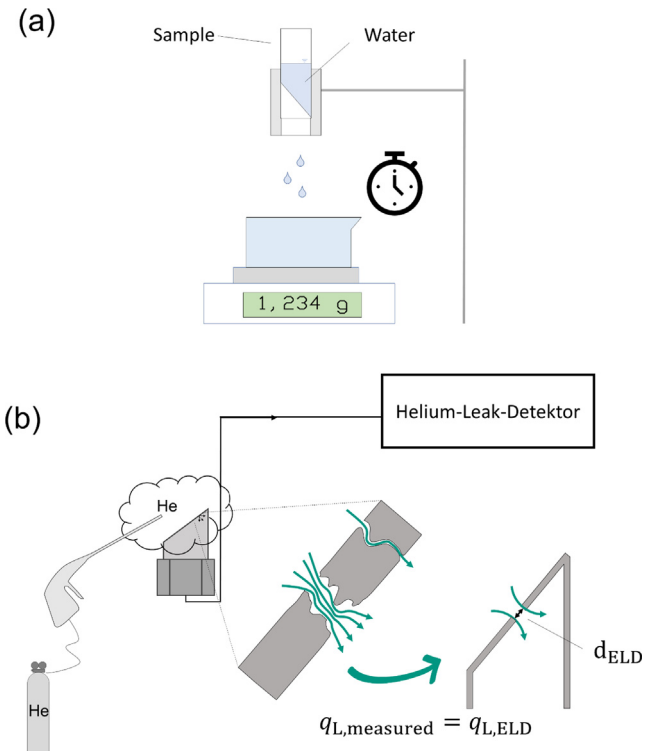

Fig. 4. Setup for determining the leak rate of the samples. (a) Leak rate determination with water for samples with a high defect density. (2) Leak rate determination with a Helium leak detector in the spray technique. From the leak rate an equivalent leak hole diameter d_{ELD} can be estimated. [45].

2.2.2. Surface texture

To characterize the surface topography, surface scans were done with a 3D optical microscope (S neox, Sensofar, Spain) in confocal fusion mode. Every surface was characterized with measurements taken on five different locations (top, bottom, left, right, center) on the inclined top surface with an area of 3.0 × 2.3 mm^2 each. The metrology software MountainsMap (Ver 8, Digital Surf, France) was used for filtering the captured data in order to retrieve the surface roughness parameters according to ISO standard 25178 [48]. An S filter of 2.5 µm was used in order to filter the small-scale components of the surface textures, followed by an L filter of 0.25 mm which removes the large-scale components. An F operator was also used in order to remove the form and leveling the surface by subtracting the least-squares mean plane.

The surface and cross sections of selected samples were also analyzed by SEM micrographs (JSM-6300 with a 10-kV beam JEOL GmbH, Germany). The cross cuts were prepared by mounting in resins, cutting and polishing. The wall thickness was determined from the SEM images using Matlab 2020a (Mathworks, USA).

2.3. Laser beam powder bed fusion system and material

In this study the PBF-LB/M printer Realizer 125 (DMG Mori, Germany) was used. The system is equipped with an 400 W Yttrium fiber-laser and an F-ϑ-lens system as well as an internal powder recycling system including an ultrasonic sieve. For this study rubber-recoated blades were used for powder spreading and recoating. The rectangular building platform has a size of 125 × 125 mm^2. Stainless steel 316l powder with a particle size of 10 – 45 µm was used (Carpenter Additive, UK). No heat treatment was performed before removing the samples from the build plate.

2.4. Scan strategy

Here it was intended to apply a scanning pattern that can be easily adapted using the generic software of the printer without the need to adopt further specific software for generating the laser paths, as has been done previously for our thin-walled parts [49,50]. Therefore, a scanning strategy only using the beam compensation function and standard laser parameters was adopted. The exact parameters are provided in the following section. Slicing

Table 1
Assumed values for the conversion of the water leak rates into a standard Helium leak rate by Eq. (1). Values from [47].

Parameter	Value
μ_{H_2O} (Pa s-1)	$1 \cdot 10^{-3}$
μ_{He} (Pa s-1)	$1.8 \cdot 10^{-6}$
Δp_{H_2O} (mbar)	0.5 (~5 mm hydrostatic water pressure)
$p_{1,He}$ (mbar)	1013
$p_{2,He}$ (mbar)	0

and calculation of the paths was done with the RDesigner Software (DMG Mori, Germany).

A double pass scanning strategy was used. As the focus is on thin-walled structures, only the inner and outer contour lines were scanned with no hatch or fill lines. The outer contour line was scanned first, then the inner contour line was scanned. These steps were then repeated in a second scan pass for each layer. The distance between two scanning lines is defined by the beam compensation and the distance in the CAD model/STL-File as shown in Eq. (3) and Fig. 5 with the definition of the wall thickness in Fig. 3.

$$d_{ss} = d_{wall,\,STL} - 2 \cdot \frac{d_{BC}}{2} \tag{3}$$

Where d_{SS} denotes the scan spacing, $d_{wall,\,STL}$ the diameter of the wall in the STL-file (green dotted lines in Fig. 5) and d_{BC} the assumed beam diameter used for the beam compensation (yellow circle in Fig. 5).

With this approach it is possible to directly influence the scan spacing of the laser paths in the CAD model by increasing or reducing the apparent wall thickness and therefore influencing the scan strategy (red lines in Fig. 5). The wall thickness in the CAD model can then be viewed rather as a scan parameter, than the actual wall thickness respectively melting width (grey dotted line in Fig. 5). This is because the actual width of a thin wall is defined by the laser parameters rather than the CAD model. The aim of this study was to find suitable parameters and specify the correct scan spacing for various inclination angles.

2.5. Experiments

It is expected to be much more difficult to achieve gas-tight, thin walls for lower inclination angles, therefore a DoE approach was chosen to first find suitable process parameters for α = 30° (see also Fig. 3) overhangs. The central composite method (see Table 5) was followed to conduct the experiments. This allows to examine the effect of the parameters sufficiently with a limited number of trials. The starting values were set based on experience [49,50] and apply a lower energy density compared to the standard parameters of the machine manufacturer.

Two phases of experimental trials with different energy density ranges were conducted, with some parameters being kept constant over all trials (see Table 2). The first trials conducted as a screening test to determine a nominal working range of the process parameters (see Table 3). This led to the processing window which was then further analyzed through a systematic Design of Experiments as shown in Table 4.

Scan speed, laser power, and scan spacing were chosen as varied parameters. The analysis was done with the DoE app in Origin 2021b (OriginLab, USA). The positions of the trials on the building platform were randomized. The whole combination of parameters of the central composite design was repeated three times, and average values were determined to compensate for experimental uncertainty. Finally, samples with smaller inclination angles were printed three times with the scan spacing and parameters given in Table 6.

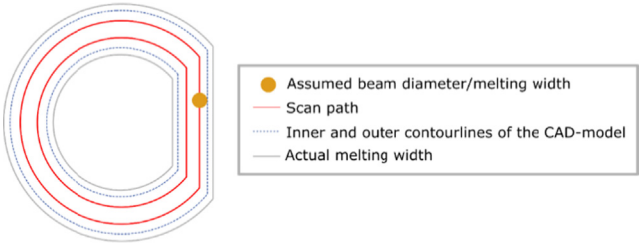

Fig. 5. Schematic representation of the scan strategy.

Table 2
Parameters kept constant for the screening test and the final DoE.

Fixed Parameters	Value
Point distance d_P (µm)	10
Focal position (mm)	0.2
Preheating	None
Layer height (µm)	50
Laser spot size (µm)	34
Inclination angle α	30

2.6. Line energy

The specific energy input is characterized by the line energy (E_l) in J m^{-1} following Eq. (4).

$$E_l = \frac{P_{Laser}}{v_s} \tag{4}$$

where P_{Laser} denotes the power of the laser and v_s the speed of the laser calculated according to Eq. (5).

$$v_s = \frac{d_P}{t_s} \tag{5}$$

with d_P as point distance and t_s exposure time.

2.7. Repeatability

In order to provide a probability-based measure of repeatability, the best performing process parameter combinations were used for printing numerous times in various locations within the build platform and as part of other build jobs during the daily usage of the printer. To remove the influence of the position, 5, respectively 10 samples were also built on one building platform in one job without any other parts.

3. Results and discussion

In this section the results of the leak rate, surface roughness measurements and the repeatability of well performing parameter sets are discussed for samples with a 30° inclination angle. The reasons for defects are analyzed then with the help of SEM images of cross cuts. Finally, the results for the parameters with higher inclination angles and a case study are reported.

3.1. Leak rate

Looking at the combined process parameter line energy for the leak rate of both the screening and the final DoE samples in Fig. 6, the correlation between leak rate and line energy is visible. With increasing line energy, the logarithmic leak rate is nearly linearly decreasing, which can be observed especially for low line energy values of the screening tests. This is the reason why the range of the systematic DoE was extended to higher line energies. Already with this second iteration, we could generate gas tight samples. In general, gas-tight samples were obtained with a line energy above approximately 320 Jm^{-1}. However, the logarithmic leak rate is quite scattered for higher energies but still within a better range of tightness as for lower energies. The scattering is expected and has intrinsic reasons based on the method of characterization of the nearly gas-tight samples. The influence of the first defect on the leak rate is quite high. Assuming a sample with one hole of, e.g., 10 µm in diameter, this hole increases the leak rate from < 10^{-8}

Table 3
Process parameters and levels for the first screening tests. (*) Due to geometric derivatives trough the discretized STL-file a scan spacing of 5 µm is the lower limit of the scan spacing in the software.

Process Parameters	Level				
	−1	−0.59	0	0.59	1
Laser power (W)	60.0	63.1	67.5	71.9	75.0
Scan speed (mm s^{-1})	250	350	500	640	750
Scan spacing (µm)	5 (*)	12	30	48	60
Beam compensation (µm)	175	168	150	132	120

Table 4
Process parameters for the final Design of Experiments plan. (*) Due to geometric derivatives trough the discretized STL-file a scan spacing of 5 µm is the lower limit of the scan spacing in the software.

Process Parameters	Level				
	−1	−0.59	0	0.59	1
Laser power (W)	60.0	68.2	80.0	91.8	100
Scan speed (mm s-1)	100	160	250	340	400
Scan spacing (µm)	5(*)	12	30	48	60
Beam compensation (µm)	175	168	150	132	120

Table 5
Used central composite design with 10 repetitions of the centre point (CP). Levels are given in Table 3 and Table 4.

	Level		
Trial	Laser power	Scan Speed	Scan spacing
1	−1	0	0
2	−0.59	−0.59	−0.59
3	−0.59	−0.59	0.59
4	−0.59	0.59	−0.59
5	−0.59	0.59	0.59
6	0	−1	0
7	0	1	0
8	0	0	−1
9	0	0	1
10–19 (CP)	0	0	0
20	0.59	−0.59	−0.59
21	0.59	−0.59	0.59
22	0.59	0.59	−0.59
23	0.59	0.59	0.59
24	1	0	0

Table 6
Experimental plan for the analysis of the influence of the angle and scan spacing.

Parameter	Value
Power (W)	80
Scan speed (mm s^{-1})	250
Angle (°)	30, 45, 60
Scan spacing (µm)	5, 12, 30, 48, 60, 72

l mbar s^{-1} (lower limit) to about 10^{-2} l mbar s^{-1}. Therefore, if the number of pores is close to zero, the value of the leak rate is discretized between the leak rate of one hole and the lower detection limit of 10^{-8} l mbar/s. In this range, the leak rate should be rather interpreted as the probability of a defect. It was consequently decided to focus the evaluation with the found parameter sets of (nearly) gas-tight walls on the reproducibility of the results.

A detailed evaluation of the DoE results illustrated in Fig. 7, leads to the following conclusions: An increase in the laser power or reduction in the scan speed applied in the PBF-LB/M process results in a decrease of the leaking rate within the inclined thin wall surface. This finding is in good agreement with previous work on integral factors like density or porosity [51]. The overall energy input on the powder is increased and enables the complete melting

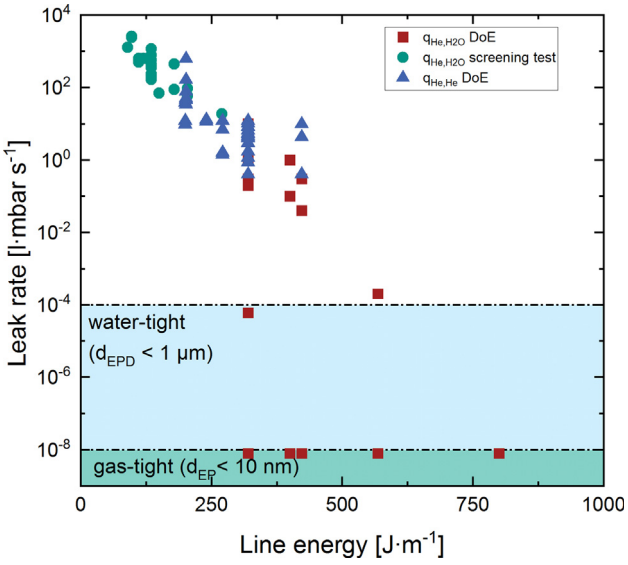

Fig. 6. The effect of line energy on the leak rate and the equivalent pore diameter according to Eq. (2) for the screening test and the DoE. $q_{He,H2O}$ denotes leak rates determined with water. For the parameters resulting in nearly gas-tight samples, Helium leak tests were conducted with adapted samples as well ($q_{He,He}$).

of the powder particles, which, due to lowerviscosity of higher energy melt, have a better wettability and form smoother surfaces as a result [17]. The samples with the highest line energies showed signs of overheating indicating the upper limit of the process window. We therefore assume that we are close to the optimum and a further search in these directions was not promising. The main effects plot is indicating that lower scan spacing would be preferably. However, interacting effects are apparent in the interaction plot since the lines are crossing. For higher powers or lower scan speeds, the effect of scan spacing is inversely proportional to the scan speed and the power, and a higher scan spacing is preferable (Fig. 8 (b), (c), (e) and (f)). This finding is coherent since a higher energy input causes a broader melt pool, and therefore a larger distance between scan vectors is preferable [17,18].

3.2. Surface roughness

Fig. 9 depicts the dependence of the surface roughness on the line energy as a power input. It can be clearly seen that the mea-

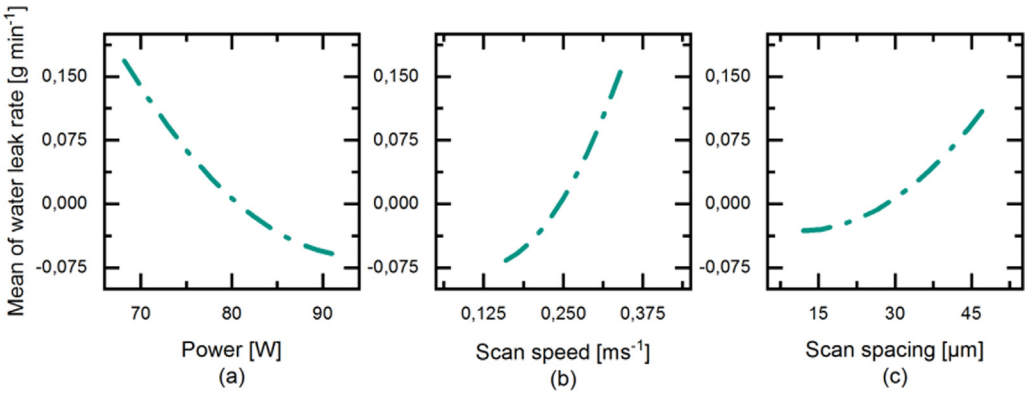

Fig. 7. Main effects plot of the process parameters (a) power, (b) scan speed and (c) scan spacing on the water leak rate evaluated as a full quadradic DoE model.

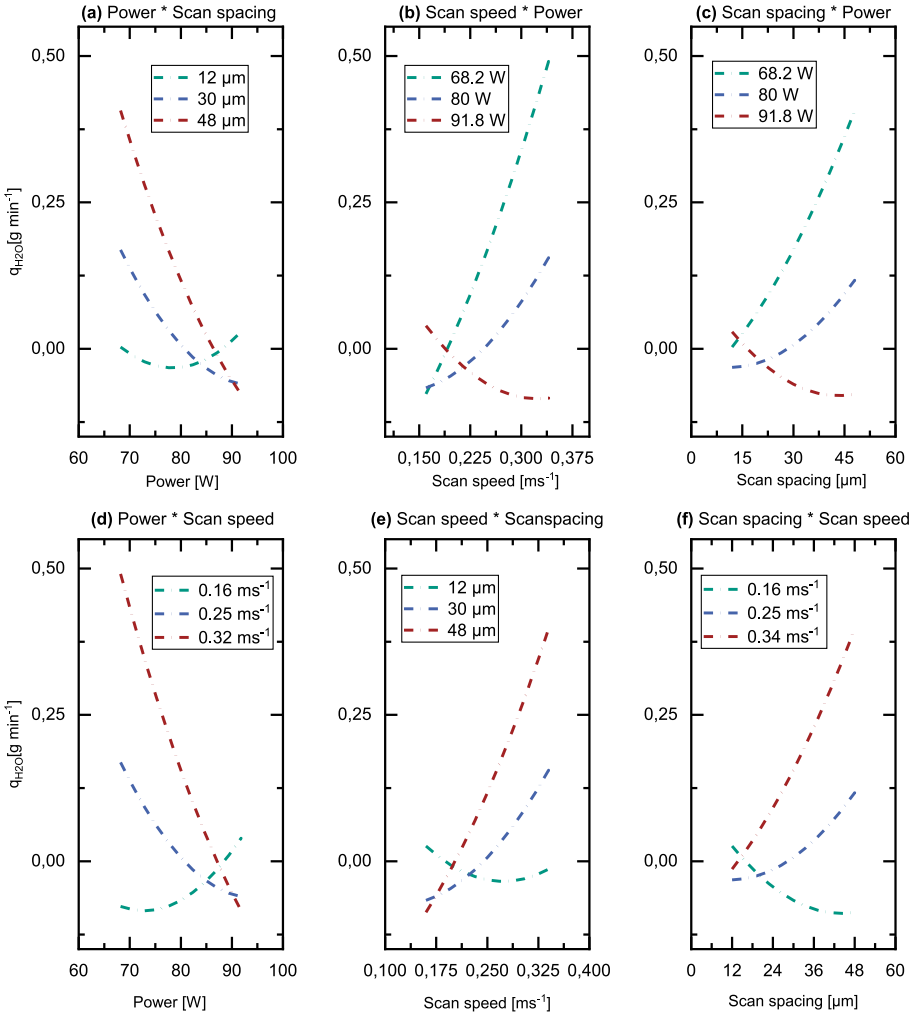

Fig. 8. Interaction plot of the scan spacing and the scan speed, respectively the laser power for the leak rate of the DoE plan from Table 4.

sured surface roughness is strongly scattered between the print jobs. Between the three repetitions of the DoE, an absolute difference in the range of the surface roughness is obvious, so is the roughness in Rep. 1 much higher than in Rep. 2 and 3. Whereas in the third repetition, marked by green downfacing triangles in Fig. 9, all S_a values are below 30 µm. This was only the case for a few high energy samples of the first repetition. The average surface roughness over all samples was much higher for this run. This highlights the problem of the repeatability of such thin walls with the PBF-LB/M process (compare also section 3.4). There are factors influencing the print in general which are not included in the study like the influence of the (rubber) recoater or the gas flow (for an extensive review see [52]), and the surface roughness is an overall factor to judge the print job quality [18]. The same general trends

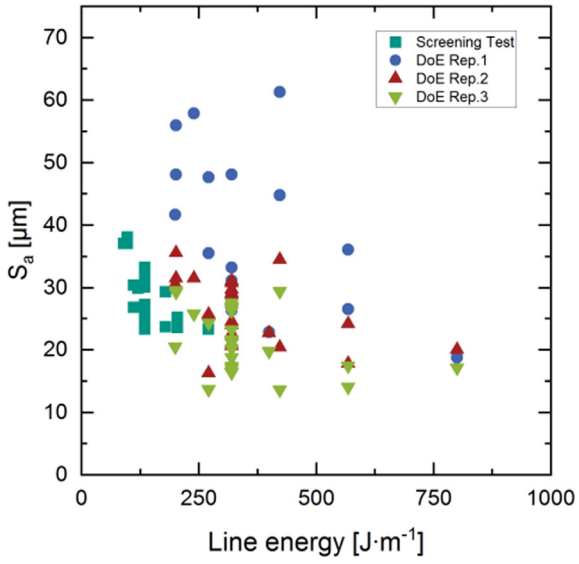

Fig. 9. The effect of line energy on the measured surface roughness S_a for the first screening test and DoE. It can be seen, that the values are quite scattered especially between repetitions, showing influences on the whole print job.

seen for the leaking rate are also seen in the evaluation of the DoE for the surface roughness (the results are given in the appendix in Fig. 19).

3.3. Repeatability

Repeatability of PBF-LB/M systems is a known issue, especially while operating at the limits of the technology, which is what this study touches upon. This is due to the impact of many influencing process parameters, their interactions, and the various processing steps [23,25]. This can be inferred from Table 7, where, with the same process parameters, some samples were not always gas-tight (such as samples 3, 9, 21 or 24) and displayed slightly different levels of tightness. It is clear from this table and also from Fig. 6 that there are influences on the whole build job which do not depend on the process parameters studied. In the first print repetition of the most promising DoE samples according to the Helium leak test results, all tested parameters except the center point showed gas-tight walls. This was not the case in the two further repetitions. Among the repeated runs, the samples produced with high line energy, in particular samples 6 and 20, produced leak-free specimens in all three repetitions. This again indicates the significant influence of the line energy on the tightness of the produced samples. The (microstructural) reasons for the low repeatability are discussed in more detail in the following section.

To further gain insight into the repeatability, parameter sets 3 and 9 were used for printing several times on the same building platform with different other parts as well as together within one build job. Parameter sets 3 and 9 were chosen, because they resulted in the thinnest walls with a reasonable probability for a leak-free sample at the same time. Looking at the results in Table 8, the probability for a leak-free wall with parameter set 9 seems better than with parameter set 3. It is also interesting to take the 9 central point measurements from Table 7 into account. The influence of the scan spacing is shown, since the difference between the central point and the parameter set 9 is only the increased scan spacing from 30 µm to 60 µm. This underlines the influence of the scan spacing which was already found in the DoE analysis (see section 3.1).

It is worth stating that the highest leak rates of the leak samples of PS 3 and 9 were in range of 10^{-1} to 10^{-4} l mbar s^{-1} representing an equivalent pore diameter in the range of 10^{-5} to 10^{-7} m (Eq. (1)). To further investigate the position and number of the holes, a bubble test was performed in order to determine the location of the leaks. With the exception of one of the central point parts of Table 7, all leaks were found on the edge of the top surface. The majority of the leaking samples had between one to three defects on the top edge of the cut through the cylinder as shown in Fig. 10 for of the specimens of parameter set 3. This also indicates that the design of walls without sharp edges is essential here even more than in standard additive manufacturing.

The following conclusion could be drawn so far: First, the results highlight the extraordinary requirements gas/liquid-tight thin walls place on fault tolerances and also on the design. Second, it shows that it is possible to print gas-tight walls with an inclination angle of 30° without any defects in the inner region.

3.4. Cross cuts

The cross-sectional SEM images show various artifacts and peculiarities that affect the quality of an inclined thin-walls, as can be found in Fig. 11. These artefacts - though not uncommon [52] especially on down-skin surfaces [53] - play a larger role due to the sensitivity of thin walls for leaks and help to understand reasons for the limited repeatability.

In Fig. 11 (a) the cross cut of a center point sample of the low energy screening test is shown. It confirms that the high leaking rate is caused by a lack of fusion of the inclined wall. In the straight circular wall only a few partly melted powder particles are adhered on the side, whereas the overhanging wall is irregular in shape with a lot more dross formation and sagging. The reason for which is the keyholing effect [53] of the melt, which can be explained by the fact that distance δ between the tracks of two consecutive layers increases with decreasing overhang angle as shown in Fig. 12 and Eq. (6) and thus reducing the overlap. From this simple geo-

Table 7
Results of the He leak rate measurements in l mbar s^{-1} for three (I, II, III) builds with selected parameter sets of the DoE plan (3, 6, 9, 3 × CP (central point), 20, 21, 24).

Parameter set	I	II	III
3	$< 10^{-8}$	$4 \cdot 10^{-2}$	$3 \cdot 10^{-1}$
6	$< 10^{-8}$	$< 10^{-8}$	$< 10^{-8}$
9	$< 10^{-8}$	$> 10^{0}$	$6 \cdot 10^{-5}$
CP 1. sample	$2 \cdot 10^{-1}$	$> 10^{0}$	$3 \cdot 10^{-1}$
CP 2. sample	$3 \cdot 10^{-1}$	$> 10^{0}$	$> 10^{0}$
CP 3. sample	$2 \cdot 10^{-1}$	$> 10^{0}$	$> 10^{0}$
20	$< 10^{-8}$	$< 10^{-8}$	$< 10^{-8}$
21	$< 10^{-8}$	$2 \cdot 10^{-4}$	$< 10^{-8}$
24	$< 10^{-8}$	$> 10^{0}$	$1 \cdot 10^{-1}$

Table 8
Summarized results of the repetition measurements of parameter sets 3 and 9 including the result of Table 7.

	Parameter set	
	3	9
Repetition on different building plates including Table 7	5 out of 8 were gas-tight (62.5%)	7 out of 8 were gas-tight (87.5%)
Repetition on different positions with 5 (I) and 10 (II) samples each in one print job	I: 3 out of 5 were gas-tight (60%) II: 3 out of 10 were gas-tight (30%)	I: 4 out of 5 were gas-tight (80%) II: 8 out of 10 were gas-tight (80%)
Overall occurrence	11 out of 23 were gas-tight (48%)	18 out of 23 were gas-tight (78%)
Overall probability p_{Leak} for at least one hole (95 % confidence)	0.522 [0.306 – 0.696]	0.217 [0.0746 – 0.615]

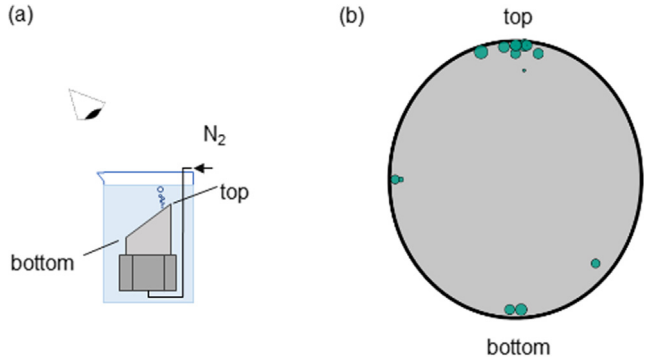

Fig. 10. (a) Experimental procedure for determining the position of the leaks. (b) Position of the leaks of all samples printed with parameter set 3. The green circles indicate the bubble size (and not the probability of occurrence) and the position of the leaks.

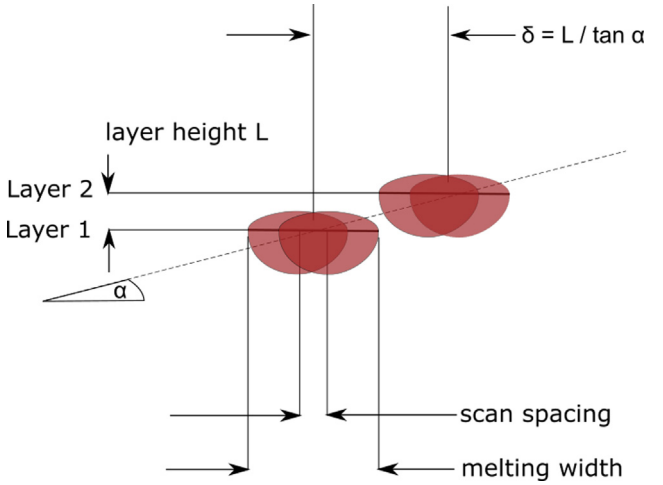

Fig. 12. Influence of overhang angle on distance between melt tracks between two layers resulting in a lack of fusion.

metric consideration, the distance δ is 87 µm with a layer height of L = 50 µm and an inclination angle α of 60°.

$$\delta = \frac{L}{\tan(\alpha)} \tag{6}$$

The low line energies of the screening tests result in smaller melt pools that do not overlap sufficiently to connect to the material underneath. The highly flowable melt rather flows in the powder bed, where it is partially melting powder particles and forming dross [53].

With increased line energy of the DoE center point samples the cross-cut images show a better fusion and less dross due to the broader melt pool as seen in Fig. 11 (b). However, there was a single artefact found, which shows also lack of fusion with clear open porosity. Potential reasons for such a defect are minor a-priori powder quality issues such as agglomeration and impurities due to recycling, or minor defects on the recoater. For example, the used Realizer machine has as an internal powder recycling system, which is why the powder quality may be affected by previous print jobs. Earlier studies with a similar machine and 316l powder showed only a small influence on the powder quality through the recycling [54]. However, other studies showed an influence of the powder depending on the number of recycling cycles [52,55,56]. Mentioning especially that powder quality is influenced in many ways, therefore making it difficult to identify the reasons [52,55,56]. Since the current study focusses on inclined thin walls, the effect of small powder quality issues like single small agglomerates or irregular shaped particles may be larger and could be a reason for the lack of fusion in Fig. 11 (b).

Further, these defects occur mainly on the top edges of the samples, so they can also be explained by the fact that the walls are closer together there. This could cause the powder to be distributed unevenly by the recoater and also spatters of the nearby melt track could negatively affect the powder bed [52].

Fig. 11 (c) depicts the joining of the inclined surface and the vertical wall for a PS 3 sample. Here an edge effect can be seen that is

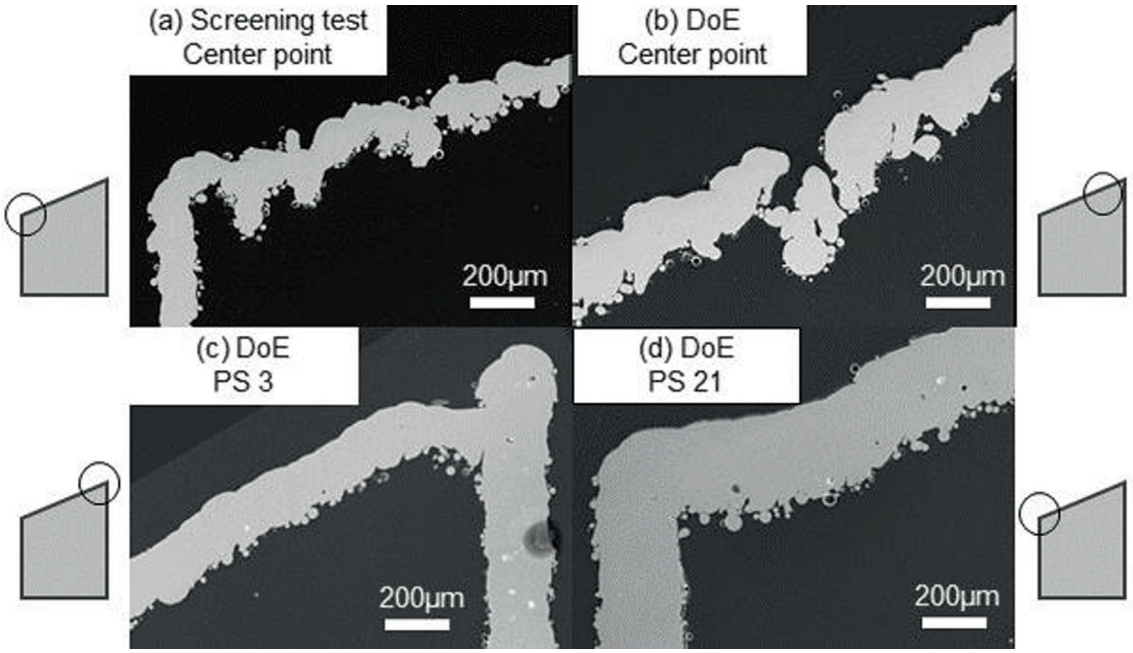

Fig. 11. Exemplary cross cuts of different defects and form deviations on different locations of the samples. In (a) lack of fusion (printed with parameter set 3), (b) artefact with lack of fusion printed with parameter set 3 (c) form deviation on top (parameter set 3) (d) deformation with parameter set 21.

caused by a sudden increase in thermal conductivity upon contact with the circular wall. The heat from the melt as well as the mass itself is transferred to the base plate through the circular wall rather than the melt flowing down into the powder bed. This results in the phenomenon where the inclined surface flows slightly downward and into the circular wall. This may lead also to cracking or lack of fusion in this area as shown in more detail in Fig. 13 (b) and also on a DoE center point sample (Fig. 13 (a)). These explanations given for Fig. 11 (b) and (c) are in line with the results of the bubble tests, presented in Fig. 10, where most of the leaks where on the top edge.

Fig. 11 (d) shows typical dross formation on the downfacing surface and in addition, a sagging phenomenon is also visible. The printed layers clearly deviate from the design dimensions. This is due to higher laser power from the parameter set 21 which results in a flowable melt pool [57]. Thin walls tend to have higher deviations due to thermal stresses and mechanical forces [20,24,31,32]. This effect is increased due to the higher temperature of the melt flow over the regions that are not supported by solid material. This causes a relative shift of the printed layer in comparison to the CAD design. This phenomenon starts within the first few overhanging layers, and as subsequent layers are melted over the previous layer, there is an aggregate shift of the whole inclined surface as can be seen in Fig. 11 (d).

Furthermore, the investigated samples tended to deform in the process of removal from the building plate. This was, however, mainly due to the low wall thickness and the low strength and not to the PBF-LB/M process itself. This underlines that for the printing of thin-walled structures stiffening through the shape is important and sharp edges should be avoided. In particular since other geometries, especially straight walls, may tend to deform by thermal stress [24].

3.5. Wall thickness

In Table 9 and Fig. 15, the results of the wall thickness/melting width measurements from the cross sections are given. As expected, the melting width and the corrected track width according to Fig. 14 is increasing with higher energy input. The scan spacing for parameter sets 3 and 9 is in the range of 30 % of the track width. Compared to the distance δ (compare Fig. 12 and section 3.4) the melting width is roughly three times larger for these parameters resulting of a horizontal overlap of around 60 – 70 % between the layers. The results show that a lower defect density comes at the price of a higher wall thickness due to the need of a significant overlap. Sample 3 and 9 have a wall thickness in the range of $2 \cdot 10^{-4}$ m whereas the gas-tight samples in all trials (parameter sets 6, 20, 21 compare also Table 7) have wall thicknesses in the range of $3 \cdot 10^{-4}$ m. These findings explain also the positive

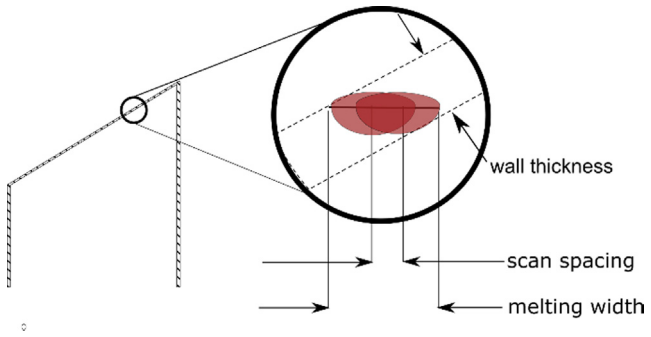

Fig. 14. Figure depicting the scan spacing and melting width as seen in Table 9.

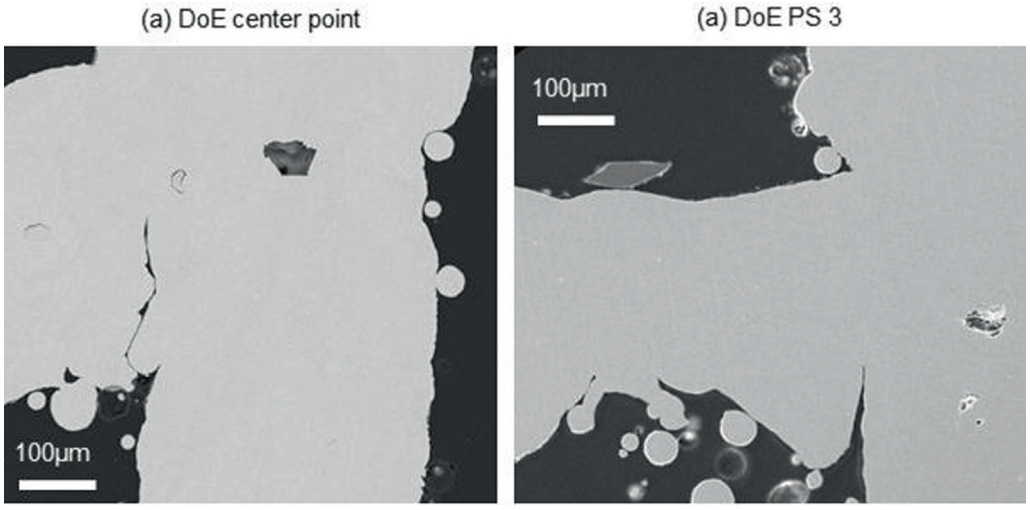

Fig. 13. Lack of fusion at the top edge of samples.

Table 9
Measured wall thickness as shown in Fig. 14 for different parameter sets of DoE of the 30° inclined walls from the SEM cross cuts.

Parameter set	E_l (J m^{-1})	Scan spacing (µm)	Wall thickness (µm)	Melting width (µm)	Track width = melting width – scan spacing (µm)
3	426	48	201	232	184
6	800	30	283	327	297
9	320	60	216	249	189
20	574	12	280	323	311
21	574	48	303	350	302

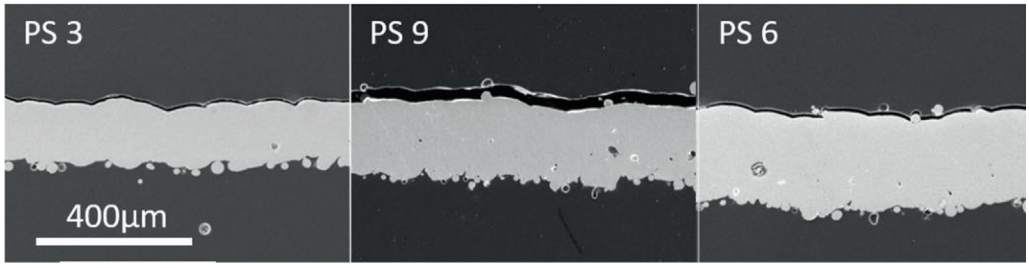

Fig. 15. SEM images of the inclined walls for the parameter sets 3, 6, 9.

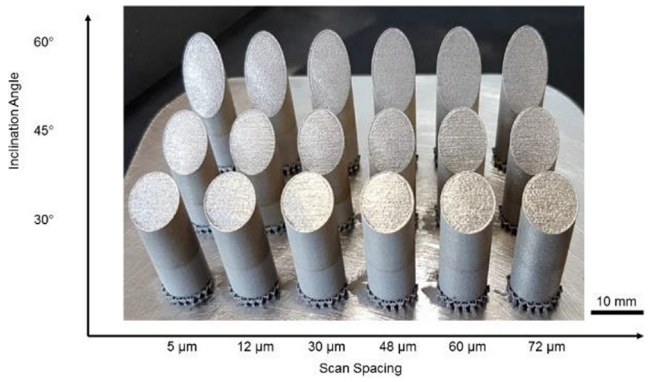

Fig. 16. Samples with different inclination angles and scan spacings as printed. All samples printed with constant laser power P_{Laser} = 80 W and a scan speed of 0.25 ms^{-1}.

influence of the scan spacing, as an increased scan spacing is increasing the melt width.

It is therefore important to find a suitable compromise between the required wall thickness (and performance), the expected defect density, and the probability of leaks. In some cases, e.g. Air-Air-heat exchangers, a minor leak rate is acceptable, and the higher performance through the lower heat resistance overcompensates the leak. In other cases, such as the distillation apparatus, this is not acceptable and would cause a failure of the system.

3.6. Influence of inclination angles

The next step was the identification of a suitable scan spacing for different inclination angles. Parameter set 9 (laser power of 80 W and scan speed of 0.25 ms^{-1}) was chosen for the printing of the test samples due to the low wall thickness and the acceptable risk for a leak. The scan spacing was varied to confirm an assumed influence of the scan spacing and the inclination angle. This parameter could also be influenced easily with most CAD systems depending on the angle.

As expected, the surfaces are much better with higher inclination angles such as 60° (see Fig. 16). Leak rate tests showed that all trails with higher inclination angles could be considered gas-tight regardless of the scan spacing. However, the trials for 30° reinforced the assumption that through the wider melt pool with a wider scan spacing a better overlap is reached. Since the samples with low scan spacing < 48 µm were leaking in all three print repetitions, whereas above that scan spacing two out of the three printed samples were gas-tight.

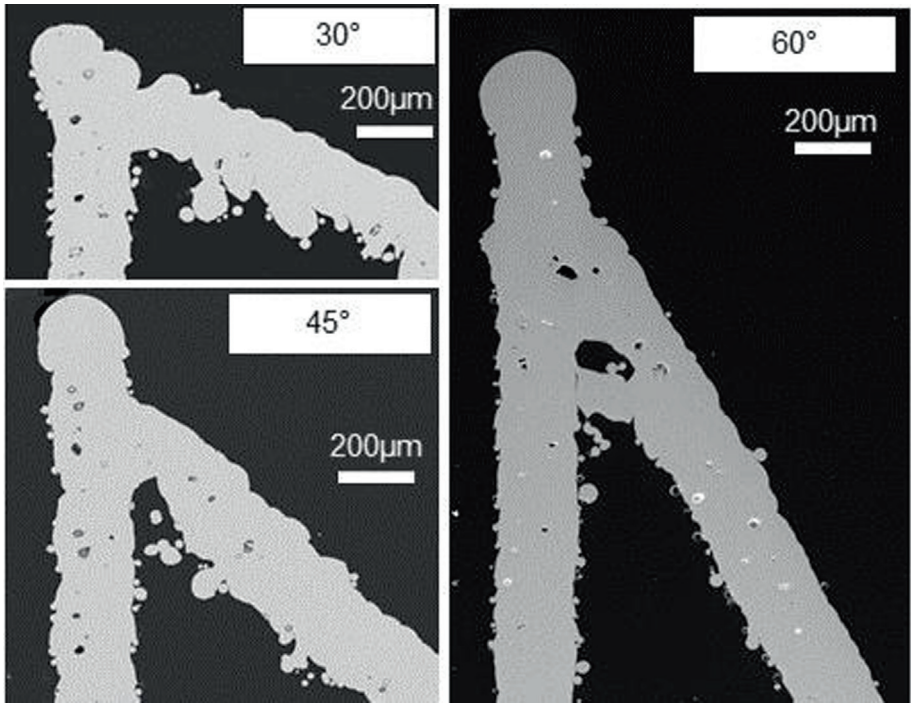

Fig. 17. SEM images of the cross cuts for different inclination angles.

Fig. 18. Printed distillation apparatus with a laser power of P_{Laser} = 80 W, a scan speed of v_s = 0,25 ms^{-1}, and a scan spacing of d_{ss} = 72 µm, resulting in gas-tight thin walls.

In Fig. 17 cross cutes of the samples with a scan spacing of 72 µm are shown. The morphology emphasizes the explanations given in section 3.4. With increased inclination the dross formation is reduced. Nevertheless, even though the 45°- and 60° samples showed no leak, the structure is irregular in the top corner on the down facing side. Highlighting again the fact, that sharp edges should be avoided by design. Furthermore, this parameter set showed also a number of closed circular pores especially in the straight walls. The closed pores are tolerated because our application does not impose mechanical stress on the part. Angular depended parameters could help to prevent this effect.

3.7. Case study

With the results of section 3.6 a promising parameter set for the print of the distillation devices were found. As the surface area in the device is much higher than of the test samples, the tilt angle was set to 45° to reduce the risk of defects. With laser power of P_{Laser} = 80 W, a scan speed of v_s = 0.25 ms^{-1}, and a scan spacing of d_{ss} = 72 µm it was possible to print the thin-walls of the device shown in Fig. 18. They showed a leak rate below 10^{-8} l mbar s^{-1} and were used directly without any sealing or post processing steps.

4. Conclusions

We have emphasized the need for gas-tight thin walls in process engineering applications. Hence, in this study a double scan strategy and method for finding the optimal printing parameters is proposed to fabricate leak-free thin-walled overhangs with inclination angles down to 30° for 316l stainless steel. Starting with a DoE approach the printing process window of scan spacing, scan speed, and laser power was identified and a correlation between leaking rate and line energy was discovered within the processing window.

The specific conclusions are the following:

- It is possible to additively manufacture gas-tight walls below d_{Wall} < 300 µm, despite the low fault tolerance of this measure.
- Roughness and leak rate measurements highlight the fact, that repeatability of additive manufacturing is a critical factor.
- For the scan spacing, an overlap of 30 % showed a higher probability of defect-free samples.
- Overlap between melt tracks of two layers must be sufficient (> 60 – 70 %) to avoid lack of fusion.
- A further look on the samples shows that the design is critical since the leaks were mostly at the edges. This leads us to conclude that design for thin inclined overhangs is even more critical than in "standard" AM and therefore sharp edges should be avoided already in the design. Further area of inclined walls below 45° should be as small as possible.
- The inclination angle of 30° was the threshold above which leak free samples were found with higher probability.
- Generally, lower defect density is seen with higher wall thickness. Therefore, the relationship between desired wall thickness and the defect density needs to be considered based on the required application.

These findings open new avenues for the design and efficient manufacturing of process devices as shown in our case study. Besides increased design freedom, the reduced fabrication time and cost as well as lower material consumption might give a competitive advantage for the production of devices. This may guide further research into the scalability of such parts and lead to new industrial applications.

Data availability statement

The raw/processed data required to reproduce these findings cannot be shared at this time as the data also forms part of an ongoing study.

CRediT authorship contribution statement

Fabian Grinschek: Conceptualization, Methodology, Software, Validation, Formal analysis, Investigation, Data curation, Visualization, Writing - original draft. **Amal Charles:** Methodology, Validation, Formal analysis, Writing - original draft. **Ahmed Elkaseer:** Validation, Formal analysis, Writing - review & editing. **Christoph Klahn:** Conceptualization, Resources, Supervision, Writing - review & editing. **Steffen G. Scholz:** Resources, Supervision, Writing - review & editing. **Roland Dittmeyer:** Conceptualization, Resources, Supervision, Funding acquisition, Writing - review & editing.

Declaration of Competing Interest

The authors declare that they have no known competing financial interests or personal relationships that could have appeared to influence the work reported in this paper.

Acknowledgments

The authors would like to thank Cornelia Schorle from IMVT (KIT) for conducting the He-leak tests, Florian Messerschmidt from IMVT (KIT) for conducting the SEM images, Manuel Hofheinz und Fabian Rupp IMVT (KIT) for machining the samples and assistance with the PBF-LB/M machine. The support of our students Juan Pablo Lara Gutierrez de Velazco, Jan Matjeka and Lennart von Deyn at IMVT (KIT) in conducting the water leak tests and surface measurements is also acknowledged.

This work was funded by Deutsche Forschungsgemeinschaft (DFG, German Research Foundation) – SFB 1441 – Project-ID 426888090

Appendix

See Fig. 19.

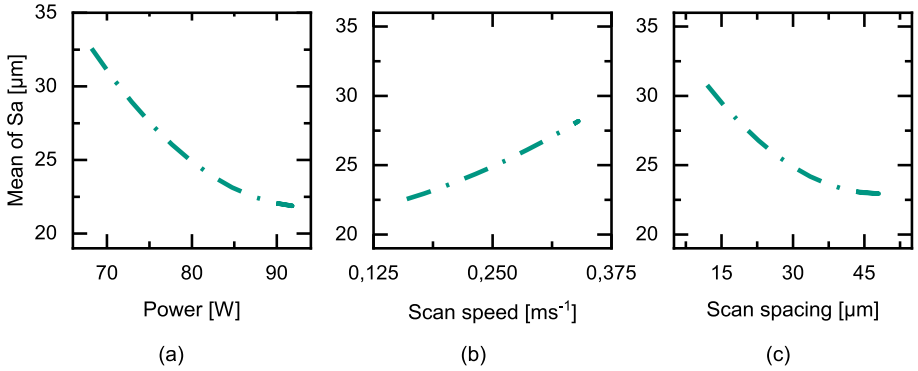

Fig. 19. Main effects plot of the process parameters. (a) power, (b) scan speed, (c) scan spacing on the surface roughness S_a with a full quadratic model.

Appendix A. Supplementary material

Supplementary data (CAD files of 45° test specimen) to this article can be found online at https://doi.org/10.1016/j.matdes.2022.111174.

References

[1] M. Schneck, M. Gollnau, M. Lutter-Günther, B. Haller, G. Schlick, M. Lakomiec, G. Reinhart, Evaluating the use of additive manufacturing in industry applications, Procedia CIRP 81 (2019) 19–23, https://doi.org/10.1016/j.procir.2019.03.004.

[2] J. Savolainen, M. Collan, How additive manufacturing technology changes business models? – review of literature, Addit. Manuf. 32 (2020), https://doi.org/10.1016/j.addma.2020.101070 101070.

[3] E. Lopez, F. Brueckner, S. Gruber, 21 - Industrial applications, in: I. Yadroitsev, I. Yadroitsava, A. Du Plessis, E. MacDonald (Eds.), Fundamentals of Laser Powder Bed Fusion of Metals, Elsevier, 2021, pp. 583–595.

[4] A. Davoudinejad, Y. Cai, D.B. Pedersen, X. Luo, G. Tosello, Fabrication of micro-structured surfaces by additive manufacturing, with simulation of dynamic contact angle, Mater. Des. 176 (2019), https://doi.org/10.1016/j.matdes.2019.107839 107839.

[5] B. Gutmann, M. Köckinger, G. Glotz, T. Ciaglia, E. Slama, M. Zadravec, S. Pfanner, M.C. Maier, H. Gruber-Wölfler, C. Oliver Kappe, Design and 3D printing of a stainless steel reactor for continuous difluoromethylations using fluoroform, React. Chem. Eng. 2 (2017) 919–927, https://doi.org/10.1039/C7RE00176B.

[6] C.H. Hornung, The art of manufacturing molecules, Science 359 (2018) 273–274, https://doi.org/10.1126/science.aar4543.

[7] C. Parra-Cabrera, C. Achille, S. Kuhn, R. Ameloot, 3D printing in chemical engineering and catalytic technology: structured catalysts, mixers and reactors, Chem. Soc. Rev. 47 (2018) 209–230, https://doi.org/10.1039/c7cs00631d.

[8] D. Xie, R. Dittmeyer, Correlations of laser scanning parameters and porous structure properties of permeable materials made by laser-beam powder-bed fusion, Addit. Manuf. 47 (2021), https://doi.org/10.1016/j.addma.2021.102261 102261.

[9] G. Kolb, Review: Microstructured reactors for distributed and renewable production of fuels and electrical energy, Chem. Eng. Process. Process Intensif. 65 (2013) 1–44, https://doi.org/10.1016/j.cep.2012.10.015.

[10] J. Singh, A. Montesinos-Castellanos, K.D.P. Nigam, Process intensification for compact and micro heat exchangers through innovative technologies: a review, Ind. Eng. Chem. Res. 58 (2019) 13819–13847, https://doi.org/10.1021/acs.iecr.9b02082.

[11] W. Podbielniak, Apparatus and methods for precise fractional-distillation analysis: new design of adiabatic fractioning column and precision-spaced wire packing for temperature range- 190° to 300° C, Ind. Eng. Chem. Anal. Ed. 13 (1941) 639–645, https://doi.org/10.1021/i560097a020.

[12] Erich Krell, Handbook of laboratory distillation, 2nd ed., Elsevier Scientific Pub. Co, Amsterdam, New York, 1982.

[13] J.J. Bower, L. Cooke, Efficient low-holdup laboratory column, Ind. Eng. Chem. Anal. Ed. 15 (1943) 290–293, https://doi.org/10.1021/i560116a028.

[14] A. Sundberg, P. Uusi-Kyyny, V. Alopaeus, Novel micro-distillation column for process development, Chem. Eng. Res. Des. 87 (2009) 705–710, https://doi.org/10.1016/j.cherd.2008.09.011.

[15] A.T. Sundberg, P. Uusi-Kyyny, V. Alopaeus, Microscale distillation, Russ. J. Gen. Chem. 82 (2012) 2079–2087, https://doi.org/10.1134/S1070363212120286.

[16] O. Diegel, A. Nordin, D. Motte, A practical guide to design for additive manufacturing, Springer Singapore, Singapore, 2019.

[17] I. Yadroitsev, I. Smurov, Surface morphology in selective laser melting of metal powders, Phys. Procedia 12 (2011) 264–270, https://doi.org/10.1016/j.phpro.2011.03.034.

[18] I. Yadroitsev, I. Smurov, Selective laser melting technology: From the single laser melted track stability to 3D parts of complex shape, Phys, Procedia 5 (2010) 551–560, https://doi.org/10.1016/j.phpro.2010.08.083.

[19] S, Clijsters, T,Craeghs, M, Moesen and J.-P, Kruth, Optimization of thin wall structures in SLM: In: Fraunhofer Additive Manufacturing Alliance (Editor): Direct Digital Manufacturing Conference 2012. Berlin, March 14th-15th, 2012.

[20] Z. Wu, S.P. Narra, A. Rollett, Exploring the fabrication limits of thin-wall structures in a laser powder bed fusion process, Int J Adv Manuf Technol 110 (2020) 191–207, https://doi.org/10.1007/s00170-020-05827-4.

[21] X. Lu, M. Chiumenti, M. Cervera, H. Tan, X. Lin, S. Wang, Warpage analysis and control of thin-walled structures manufactured by laser powder bed fusion, Metals 11 (2021) 686, https://doi.org/10.3390/met11050686.

[22] P.R. Gradl, D.C. Tinker, J. Ivester, S.W. Skinner, T. Teasley, J.L. Bili, Geometric feature reproducibility for laser powder bed fusion (L-PBF) additive manufacturing with Inconel 718, Addit. Manuf. 47 (2021), https://doi.org/10.1016/j.addma.2021.102305 102305.

[23] A. Ahmed, A. Majeed, Z. Atta, G. Jia, Dimensional Quality and Distortion Analysis of Thin-Walled Alloy Parts of AlSi10Mg Manufactured by Selective Laser Melting, JMMP 3 (2019) 51, https://doi.org/10.3390/jmmp3020051.

[24] H. Krauss, M.F. Zaeh, Investigations on manufacturability and process reliability of selective laser melting, Physics Procedia 41 (2013) 815–822, https://doi.org/10.1016/j.phpro.2013.03.153.

[25] L. Dowling, J. Kennedy, S. O'Shaughnessy, D. Trimble, A review of critical repeatability and reproducibility issues in powder bed fusion, Mater. Des. 186 (2020), https://doi.org/10.1016/j.matdes.2019.108346 108346.

[26] N. Sanaei, A. Fatemi, N. Phan, Defect characteristics and analysis of their variability in metal L-PBF additive manufacturing, Mater. Des. 182 (2019), https://doi.org/10.1016/j.matdes.2019.108091 108091.

[27] J. Riese, A. Reitze, M. Grünewald, Experimental characterization of 3D printed structured metal packing with an enclosed column wall, Chem. Ing. Tech. 94 (7) (2022) 993–1001, https://doi.org/10.1002/cite.202200002.

[28] A. Charles, A. Elkaseer, U. Paggi, L. Thijs, V. Hagenmeyer, S. Scholz, Down-facing surfaces in laser powder bed fusion of Ti6Al4V: effect of dross formation on dimensional accuracy and surface texture, Addit. Manuf. 46 (2021), https://doi.org/10.1016/j.addma.2021.102148 102148.

[29] A. Triantaphyllou, C.L. Giusca, G.D. Macaulay, F. Roerig, M. Hoebel, R.K. Leach, B. Tomita, K.A. Milne, Surface texture measurement for additive manufacturing, Surf. Topogr.: Metrol. Prop. 3 (2015) 24002, https://doi.org/10.1088/2051-672x/3/2/024002.

[30] F. Calignano, Design optimization of supports for overhanging structures in aluminum and titanium alloys by selective laser melting, Mater. Des. 64 (2014) 203–213, https://doi.org/10.1016/j.matdes.2014.07.043.

[31] T. Yang, D. Xie, W. Yue, S. Wang, P. Rong, L. Shen, J. Zhao, C. Wang, Distortion of thin-walled structure fabricated by selective laser melting based on assumption of constraining force-induced distortion, Metals 9 (2019) 1281, https://doi.org/10.3390/met9121281.

[32] A. Chakraborty, R. Tangestani, R. Batmaz, W. Muhammad, P. Plamondon, A. Wessman, L. Yuan, É. Martin, In-process failure analysis of thin-wall structures made by laser powder bed fusion additive manufacturing, J. Mater. Sci. Technol. 98 (2022) 233–243, https://doi.org/10.1016/j.jmst.2021.05.017.

[33] K. Zeng, Optimization of support structures for selective laser melting, Electronic Theses and Dissertations (2015), https://doi.org/10.18297/etd/2221.

[34] X. Wang, K. Chou, Effect of support structures on Ti-6Al-4V overhang parts fabricated by powder bed fusion electron beam additive manufacturing, J. Mater. Process. Technol. 257 (2018) 65–78, https://doi.org/10.1016/j.jmatprotec.2018.02.038.

[35] M. Biedermann, P. Beutler, M. Meboldt, Automated design of additive manufactured flow components with consideration of overhang constraint, Addit. Manuf. 46 (2021), https://doi.org/10.1016/j.addma.2021.102119 102119.

[36] A. Du Plessis, I. Yadroitsava, I. Yadroitsev, Effects of defects on mechanical properties in metal additive manufacturing: A review focusing on X-ray tomography insights, Mater. Des. 187 (2020), https://doi.org/10.1016/j.matdes.2019.108385 108385.

[37] F.H. Kim, S.P. Moylan, Literature review of metal additive manufacturing defects, National Institute of Standards and Technology, Gaithersburg, MD, 2018.
[38] A. Elkaseer, A. Charles, S. Scholz, Development of Precision Additive Manufacturing Processes, in: R.K. Leach, S. Carmignato (Eds.), Precision Metal Additive Manufacturing, CRC Press, Boca Raton, 2021.
[39] H.E. Sabzi, E. Hernandez-Nava, X.-H. Li, H. Fu, D. San-Martín, P.E. Rivera-Díaz-del-Castillo, Strengthening control in laser powder bed fusion of austenitic stainless steels via grain boundary engineering, Mater. Des. 212 (2021), https://doi.org/10.1016/j.matdes.2021.110246 110246.
[40] S. Qu, J. Ding, J. Fu, M. Fu, B. Zhang, X. Song, High-precision laser powder bed fusion processing of pure copper, Addit. Manuf. 48 (2021), https://doi.org/10.1016/j.addma.2021.102417 102417.
[41] J. Jakumeit, G. Zheng, R. Laqua, S.J. Clark, J. Zielinski, J.H. Schleifenbaum, P.D. Lee, Modelling the complex evaporated gas flow and its impact on particle spattering during laser powder bed fusion, Addit. Manuf. 47 (2021), https://doi.org/10.1016/j.addma.2021.102332 102332.
[42] C. Chen, Z. Xiao, Y. Wang, X. Yang, H. Zhu, Prediction study on in-situ reduction of thermal stress using combined laser beams in laser powder bed fusion, Addit. Manuf. 47 (2021), https://doi.org/10.1016/j.addma.2021.102221 102221.
[43] M. Slodczyk, A. Ilin, T. Kiedrowski, T. Bareth, V. Ploshikhin, Spatter reduction by multi-beam illumination in laser powder-bed fusion, Mater. Des. 212 (2021), https://doi.org/10.1016/j.matdes.2021.110206 110206.
[44] A. Suzuki, T. Miyasaka, N. Takata, M. Kobashi, M. Kato, Control of microstructural characteristics and mechanical properties of AlSi12 alloy by processing conditions of laser powder bed fusion, Addit. Manuf. 48 (2021), https://doi.org/10.1016/j.addma.2021.102383 102383.
[45] H. Rottländer, W. Umrath, G. Voss, Fundamentals of leak detection, Leybold GmbH (2016).
[46] J. Zierep, K. Bühler, Principles of fluid mechanics: fundamentals, statics and dynamics of fluids, Springer Fachmedien Wiesbaden; Imprint Springer, Wiesbaden, 2022.
[47] Verein Deutscher Ingenieure, VDI Heat Atlas, Springer Berlin Heidelberg, Berlin, Heidelberg, 2010.
[48] ISO 25178-600, Geometrical product specifications (GPS) — Surface texture: Areal — Part 600: metrological characteristics for areal topography measuring methods, 2019.
[49] E. Hansjosten, A. Wenka, A. Hensel, W. Benzinger, M. Klumpp, R. Dittmeyer, Custom-designed 3D-printed metallic fluid guiding elements for enhanced heat transfer at low pressure drop, Chem. Eng. Process. 130 (2018) 119–126, https://doi.org/10.1016/j.cep.2018.05.022.
[50] F. Grinschek, D. Xie, M. Klumpp, M. Kraut, E. Hansjosten, R. Dittmeyer, Regular microstructured elements for intensification of gas-liquid contacting made by selective laser melting, Ind. Eng. Chem. Res. 59 (9) (2020) 3736–3743, https://doi.org/10.1021/acs.iecr.9b04548.
[51] A. Charles, A. Elkaseer, L. Thijs, V. Hagenmeyer, S. Scholz, Effect of process parameters on the generated surface roughness of down-facing surfaces in selective laser melting, Appl. Sci. 9 (2019) 1256, https://doi.org/10.3390/app9061256.
[52] A. Mostafaei, C. Zhao, Y. He, S. Reza Ghiaasiaan, B.o. Shi, S. Shao, N. Shamsaei, Z. Wu, N. Kouraytem, T. Sun, J. Pauza, J.V. Gordon, B. Webler, N.D. Parab, M. Asherloo, Q. Guo, L. Chen, A.D. Rollett, Defects and anomalies in powder bed fusion metal additive manufacturing, Curr. Opin. Solid State Mater. Sci. 26 (2) (2022) 100974, https://doi.org/10.1016/j.cossms.2021.100974.
[53] A. Charles, M. Bayat, A. Elkaseer, L. Thijs, J.H. Hattel, S. Scholz, Elucidation of dross formation in laser powder bed fusion at down-facing surfaces: Phenomenon-oriented multiphysics simulation and experimental validation, Addit. Manuf. 50 (2022), https://doi.org/10.1016/j.addma.2021.102551 102551.
[54] A. Röttger, K. Geenen, M. Windmann, F. Binner, W. Theisen, Comparison of microstructure and mechanical properties of 316 L austenitic steel processed by selective laser melting with hot-isostatic pressed and cast material, Mater. Sci. Eng., A 678 (2016) 365–376, https://doi.org/10.1016/j.msea.2016.10.012.
[55] G. Jacob, C.U. Brown, M.A. Donmez, S.S. Watson, J. Slotwinski, Effects of powder recycling on stainless steel powder and built material properties in metal powder bed fusion processes, National Institute of Standards and Technology, Gaithersburg, MD, 2017.
[56] D. Powell, A.E. Rennie, L. Geekie, N. Burns, Understanding powder degradation in metal additive manufacturing to allow the upcycling of recycled powders, J. Cleaner Production 268 (2020), https://doi.org/10.1016/j.jclepro.2020.122077 122077.
[57] S. Sun, M. Brandt, M. Easton, Powder bed fusion processes, in: M. Brandt (Ed.), Laser Additive Manufacturing, Woodhead Publishing, 2017, pp. 55–77.